Available online at www.sciencedirect.com

ScienceDirect

journal homepage: www.elsevier.com/locate/he

Surface selective passivation and $Fe_xNi_{1-x}OOH$ co-modified Fe_2O_3 photoanode toward high-performance water oxidation

*Kaikai Ba, Yinyin Li, Rui Zhang, Kai Zhang, Zhijun Liang, Yunan Liu, Yanhong Lin, Dejun Wang, Tengfeng Xie**

Institute of Physical Chemistry, College of Chemistry, Jilin University, Changchun 130012, PR China

HIGHLIGHTS

- $[B(OH)_4]^-$ as a Lewis base can selectively passivate acceptor surface states.
- The $Fe_xNi_{1-x}OOH$ thin layer can further improve water oxidation kinetics.
- $Fe_xNi_{1-x}OOH/B/Ti-Fe_2O_3$ could achieve 3.39 mA/cm^2 at 1.23 V vs. RHE.
- $Fe_xNi_{1-x}OOH/B/Ti-Fe_2O_3$ exhibits the outstanding PEC performance.

GRAPHICAL ABSTRACT

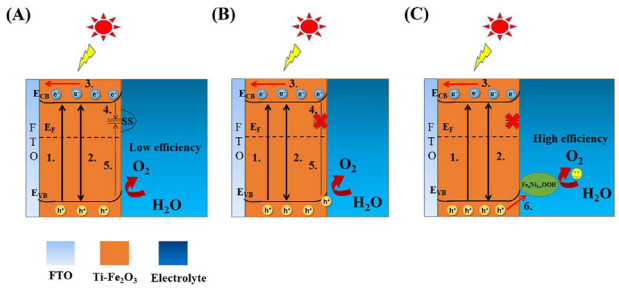

ARTICLE INFO

Article history:
Received 10 June 2022
Received in revised form
15 October 2022
Accepted 31 October 2022
Available online 16 November 2022

Keywords:
Acceptor surface states
Borate treatment
$Ti-Fe_2O_3$ photoanode
Charge separation
PEC water Oxidation

ABSTRACT

Improving the water-splitting performance of hematite (α-Fe_2O_3) is still hindered due to its severe charge recombination and poor water oxidation kinetics. Herein, borate-treated $Ti-Fe_2O_3$ combined with a $Fe_xNi_{1-x}OOH$ cocatalyst ($Fe_xNi_{1-x}OOH/B/Ti-Fe_2O_3$) greatly improved the performance of $Ti-Fe_2O_3$, and reached a notable photocurrent density of 3.39 mA/cm^2 at 1.23 V vs. RHE. Transient surface photovoltage spectroscopy (TPV) directly reveals that $[B(OH)_4]^-$ as a Lewis base can selectively passivate acceptor surface states on $Ti-Fe_2O_3$ photoanode surface, efficiently enhancing the charge separation efficiency. Moreover, the $Fe_xNi_{1-x}OOH$ thin layer is devoted to further facilitate holes injection into the electrolyte, accelerating the water oxidation kinetics of $Ti-Fe_2O_3$ photoanode. The synergetic integration of acceptor surface states passivation and $Fe_xNi_{1-x}OOH$ cocatalyst provides a novel strategy for the construction of efficient photoanodes by surface engineering.

* *Corresponding author.*
E-mail address: xietf@jlu.edu.cn (T. Xie).

https://doi.org/10.1016/j.ijhydene.2022.10.277

Introduction

As a clean and pollution-free energy source, hydrogen energy has become a research hotspot [1,2]. In particular, the use of inexhaustible solar energy to split water for hydrogen production has always been regarded as a reliable strategy with low cost [3]. As an outstanding water oxidation photoanode, hematite has been widely reported as a result of its low toxicity, sufficient edge positions of the valence band and high chemical stability in alkaline electrolytes [4,5]. However, pure α-Fe_2O_3 has abundant acceptor surface states and sluggish water oxidation kinetics, which lead to serious charge recombination on the surface and limit its PEC performance for application.

Various surface states exist on the surface of hematite [6], and it is known that the acceptor surface states usually preferentially capture photogenerated electrons on the surface and seriously recombine with the holes [7], thereby inhibiting the improvement of its PEC performance. Currently, the strategy to suppress the surface state density of α-Fe_2O_3 is mainly by decorating the surface passivation layer material, such as Ga_2O_3 [8], Al_2O_3 [9], In_2O_3 [10]and MoO_3 [11], etc. However, conventional electrodeposition or precipitation methods, which often produce thick or non-uniform overlays, can lead to non-selective passivation [12]. As the conjugate base of H_3BO_3, $[B(OH)_4]^-$ with tetrahedral geometry has been reported that it acts as a regulating ligand and passivator in the molecular level modification, rather than forming a thick surface passivation layer [13]. Zhang et al. reported that self-anchored $[B(OH)_4]^-$ ligands on $BiVO_4$ inhibit charge recombination while enhancing the transport of holes to the electrolyte [14,15]. In fact, the acceptor surface state on hematite can be regarded as a Lewis acid site, and the $[B(OH)_4]^-$ as a Lewis base will selectively bind to it. Considering the specific properties of the acceptor surface states, borate treatment should be able to passivate acceptor surface states of α-Fe_2O_3 while suppressing charge recombination. Furthermore, bimetallic oxygen evolution cocatalysts are often able to greatly promote holes transfer at the photoanode/electrolyte interface and reduce the onset potential of α-Fe_2O_3, such as ZnCo-LDH [16], FeNiOOH [17], $FeCoO_x$ [18] and $MnCoO_x$ [5,19], etc. Therefore, we can reasonably infer that the synergetic integration of acceptor surface states passivation and bimetallic cocatalysts can greatly improve the photoelectrochemical properties of Fe_2O_3 for water oxidation.

Herein we used borate solution to treat the surface of Ti—Fe_2O_3 photoanode, and the $[B(OH)_4]^-$ as Lewis base will selectively bind to acceptor surface states. The surface photovoltage spectroscopy (SPV), transient photovoltage (TPV) and necessary electrochemical measurements demonstrate that acceptor surface states on Ti—Fe_2O_3 surface are passivated, efficiently enhancing its charge separation efficiency. Moreover, the $Fe_xNi_{1-x}OOH$ thin layer is devoted to extract holes from B/Ti—Fe_2O_3 to accelerate surface reaction. The synergetic integration of acceptor surface states passivation and $Fe_xNi_{1-x}OOH$ cocatalyst provides a novel strategy for the construction of efficient PEC photoanodes.

Experimental section

Sample preparation

Preparation of Ti-doped Fe_2O_3

Ti-doped Fe_2O_3 nanorod array were prepared according to the previously reported method [20,21]. Typically, the FTO was ultrasonically cleaned with ethanol, acetone, ethyl acetate, etc. for 15 min each. 0.15 M $FeCl_3 \cdot 6H_2O$, 1 M $NaNO_3$ and 150 μL 0.05% $TiCl_4$ ethanol solution (volume percentage) were dissolved in 100 mL deionized water under constant stirring. Immediately thereafter, a piece of cleaned FTO was transferred to a 50 mL autoclave along with the homogeneous solution. The autoclave was heated in an oven at 100 °C for 12 h, cooled to room temperature, and the yellow film was removed and rinsed with deionized water. After drying, the yellow film was calcined in air at 550 °C for 2 h to obtain Ti—Fe_2O_3.

Preparation of B/Ti—Fe_2O_3

In short, the obtained Ti—Fe_2O_3 photoanode was placed in a 0.5 M borate buffer solution at 90 °C for 1 h (pH = 9.3). Finally, the resulting film was rinsed with deionized water and dried naturally and the synthesized sample is marked as B/Ti—Fe_2O_3.

Preparation of $Fe_xNi_{1-x}OOH$/B/Ti—Fe_2O_3

$Fe_xNi_{1-x}OOH$ cocatalyst was synthesized via dipping method [22]. Briefly, the B/Ti—Fe_2O_3 electrode was immersed into the mixed solution of $FeCl_3 \cdot 6H_2O$ (0.15 mM) and $NiCl_2 \cdot 6H_2O$ (0.25 mM) solution for 15 min. 2 M NaOH solution was then added to adjust its pH to 9 by gently stirring for 5 min. The solution was stood for 30 min. At last, the sample was washed with deionized water and then dried naturally to obtain $Fe_xNi_{1-x}OOH$/B/Ti—Fe_2O_3. To optimize the composition of the Ni^{2+} and Fe^{3+}, the total moles of them in the mixed solution were maintained at 0.4 mM, the molar ratio of $FeCl_3.6H_2O$ to $NiCl_2.6H_2O$ is set to 1:0, 0.625:0.375, 0.75:0.25, 0.5:0.5, 0.25:0.75, and 0:1.

For comparison, the $Fe_xNi_{1-x}OOH$/Ti—Fe_2O_3 electrode was also obtained.

Characterization

The morphologies of all photoanodes were characterized by field emission scanning electron microscopy (FE-SEM) and transmission electron microscopy (TEM). The light absorption properties of all photoanodes were characterized through ultraviolet-diffuse reflectance absorption (UV/vis DRS). The elemental compositions and their chemical states of all photoanodes were characterized by X-ray photoelectron spectroscopy (XPS) and corrected using the C1s peak. The crystal phase structures of all photoanodes were characterized by X-ray diffraction (XRD) ranging from 20 to 80°.

The dynamic separation behaviors of photogenerated charges were characterized by locking-based surface photovoltage spectroscopy (SPV) and transient photovoltage spectroscopy (TPV). The SPV test was completed from 300 to 800 nm and the test frequency was 24 Hz, which consisted of the monochromator (ZLolix SBP500), data processor, optical

chopper (SR540), lock Phase amplifier (SB830-DSP) and 500 W Xe lamp (CHF-XM-500 W). The TPV test was performed under 100 μJ laser irradiationunder (Laser wavelength: 532 nm), which consisted of the signal capture amplifier, digital oscilloscope (500 MHz, Tektronix), data processor, and pulsed laser (Polaris II, New Wave Research, Inc.).

PEC measurements

Photoelectrochemical tests were performed with simulated sunlight illumination (AM 1.5 G, 100 mW/cm^2) from the sample side, using an electrochemical station (CHI660E) configured with a standard three-electrode system, where the Ag/AgCl, photoanode and platinum wire were used as reference, working and counter electrodes. By Nernst equation ($E_{RHE-} = E_{Ag/AgCl} + 0.059\ pH + E^{\theta}_{Ag/AgCl}$) conversion, the Ag/AgCl reference electrode potential is converted to the potential relative to the standard hydrogen electrode, the electrolyte is 1 M potassium hydroxide (pH = 13.6), 0.283 square cm as the reaction area. The stability test of $Fe_xNi_{1-x}OOH/B/Ti{-}Fe_2O_3$ was carried out under the condition of 1.23 V vs. RHE continuous illumination for 2 h. PEIS was performed under light in the frequency range 5×10^{-2}-10^5 Hz (1.0 V vs. RHE).

The conversion efficiency is obtained from the relationship between incident photons and current:

$$IPCE = \frac{J \times 1240}{P_{mono} \times \lambda}$$

where λ is the irradiation wavelength, the wavelength range is 390–570 nm, P_{mono} is the light intensity, and J is the photocurrent density.

The applied bias photon-to-current efficiency (ABPE) is obtained through the following equation:

$$ABPE = \frac{(J_{light} - J_{dark}) \times (1.23 - VRHE)}{P_{light}}$$

where P_{light} represents the incident light intensity (100 mW/cm^2), V_{RHE} represents the potential relative to the standard hydrogen electrode, and J_{light} and J_{dark} represent the current density of the photoanode in light and dark states, respectively.

The injection efficiency (η_{inj}) is obtained by the following formula:

$$\eta_{inj} = \frac{J_{H_2O}}{J_{H_2O_2}}$$

where J_{H2O} and J_{H2O2} represent the photocurrent densities obtained in 1 M potassium hydroxide and its electrolyte containing 0.5 M hydrogen peroxide, respectively.

Cyclic voltammetry (CV) plots were performed in potential range of −0.4 to −0.3 V vs. Ag/AgCl at the scan rates of 0.01, 0.03, 0.05, 0.07 and 0.09 V s^{-1}, respectively.

Results and discussions

Synthesis and characterization

Scheme 1 shows the synthesis process of $Fe_xNi_{1-x}OOH/B/Ti{-}Fe_2O_3$ photoanode. Fe_2O_3 nanorod array with Ti dopant aiming to improve the conductivity, first, was synthesized on FTO. For the borate treatment, the prepared $Ti{-}Fe_2O_3$ was placed in a 0.5 M borate buffer solution for a certain time, which was labelled as $B/Ti{-}Fe_2O_3$. Finally, the $Fe_xNi_{1-x}OOH$ thin layer is modified onto $B/Ti{-}Fe_2O_3$ via pH-modulated method, and the target photoanode was marked as $Fe_xNi_{1-x}OOH/B/Ti{-}Fe_2O_3$.

From the top-view SEM of the photoanode (Fig. S1), it can be seen that $Ti{-}Fe_2O_3$ is assembled by a large number of nanorods with an average diameter of 54 nm. However, there is no apparent morphology changes after borate treatment and cocatalyst modification on $Ti{-}Fe_2O_3$. Subsequently, the microstructure and morphology of the as-synthesized $Fe_xNi_{1-x}OOH/B/Ti{-}Fe_2O_3$ were then further analyzed by HRTEM and TEM. In Fig. 1A and B, a 5 nm-thick ultrathin layer of amorphous $Fe_xNi_{1-x}OOH$ is uniformly deposited on $Ti{-}Fe_2O_3$ [15,23]. The lattice fringe of 0.254 nm displayed in the $Fe_xNi_{1-x}OOH/B/Ti{-}Fe_2O_3$ HRTEM image in Fig. 1C corresponds to the α-Fe_2O_3 (110) plane [24]. The elemental mapping in Fig. 1D clearly showed the uniform distribution of Fe, O, Ti, B and Ni in $Fe_xNi_{1-x}OOH/B/Ti{-}Fe_2O_3$, indicating further the formation

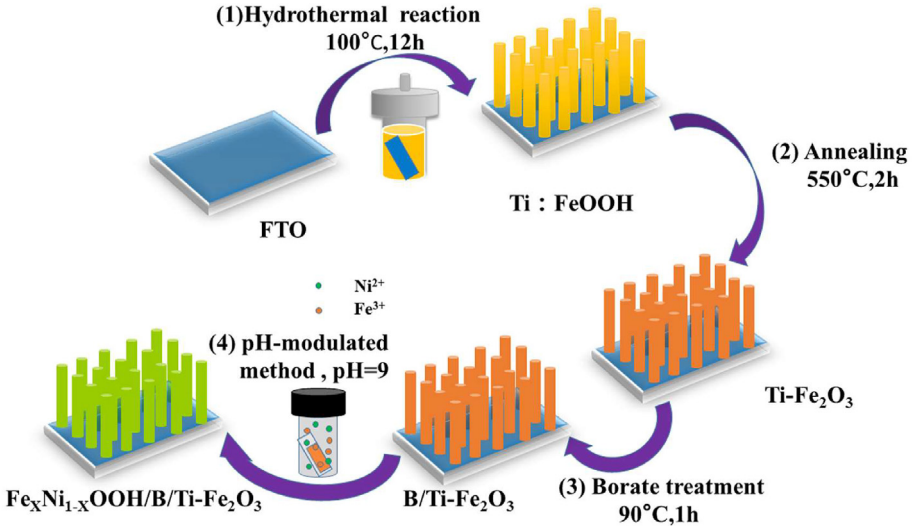

Scheme 1 – The synthesis process of $Fe_xNi_{1-x}OOH/B/Ti{-}Fe_2O_3$.

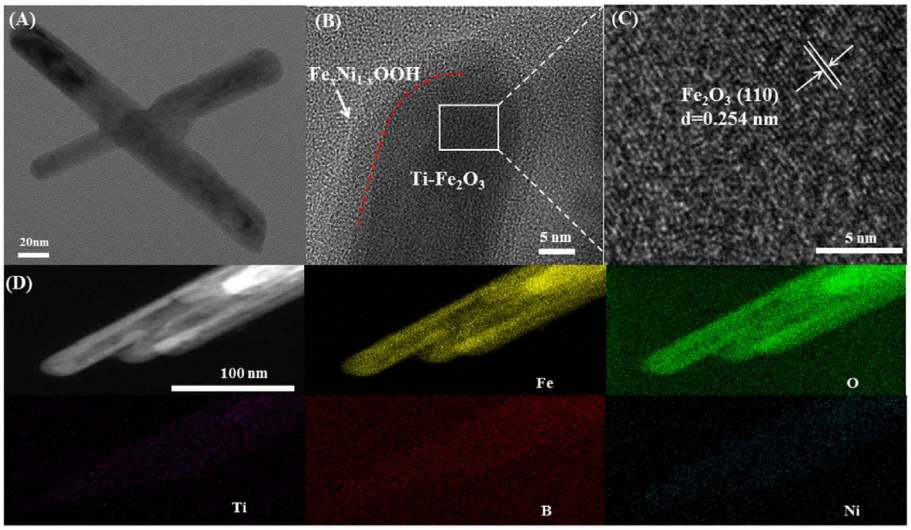

Fig. 1 – (A) TEM image of $Fe_xNi_{1-x}OOH/B/Ti-Fe_2O_3$, (B) and (C) HRTEM image of $Fe_xNi_{1-x}OOH/B/Ti-Fe_2O_3$, (D) EDS elemental mapping of Fe, O, Ti, B and Ni of $Fe_xNi_{1-x}OOH/B/Ti-Fe_2O_3$.

of ultrathin $Fe_xNi_{1-x}OOH$ nanolayers, as well as boron adsorption.

The crystalline phase of all photoanodes in Fig. 2A were investigated by X-ray diffraction (XRD) pattern. In the XRD spectra of $Fe_xNi_{1-x}OOH/B/Ti-Fe_2O_3$ and $Fe_xNi_{1-x}OOH/Ti-Fe_2O_3$, there are no other diffraction peaks except for α-Fe_2O_3 (PDF#33–0664) and FTO, which is due to amorphous structure, ultrathin thickness and high dispersion of $Fe_xNi_{1-x}OOH$ [25]. In addition, through X-ray photoelectron spectroscopy (XPS), the elemental composition of all photoanodes and their chemical states were measured. The two peaks at 710.1 eV and 723.9 eV can be observed in Fig. 2B, which are assigned to $Fe2p_{3/2}$ and

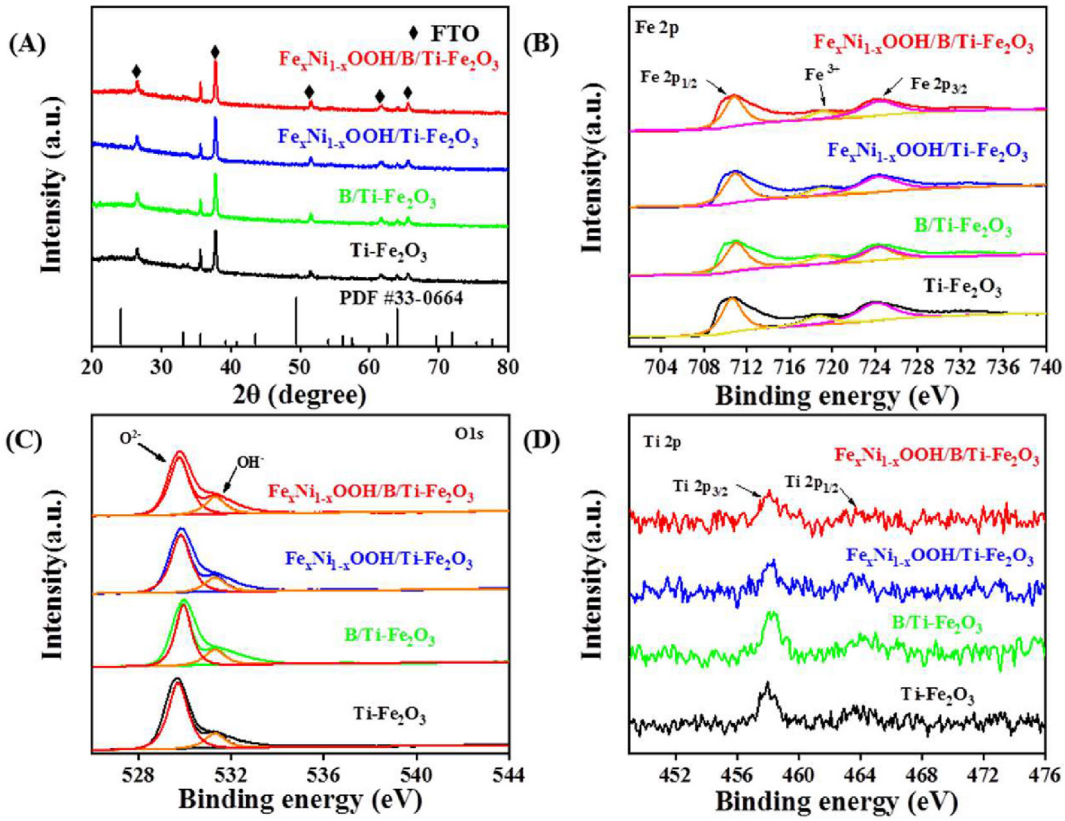

Fig. 2 – (A) XRD patterns and XPS spectra of (B) Fe 2p, (C) O 1s, (D) Ti 2p collected from $Ti-Fe_2O_3$, $B/Ti-Fe_2O_3$, $Fe_xNi_{1-x}OOH/Ti-Fe_2O_3$ and $Fe_xNi_{1-x}OOH/B/Ti-Fe_2O_3$.

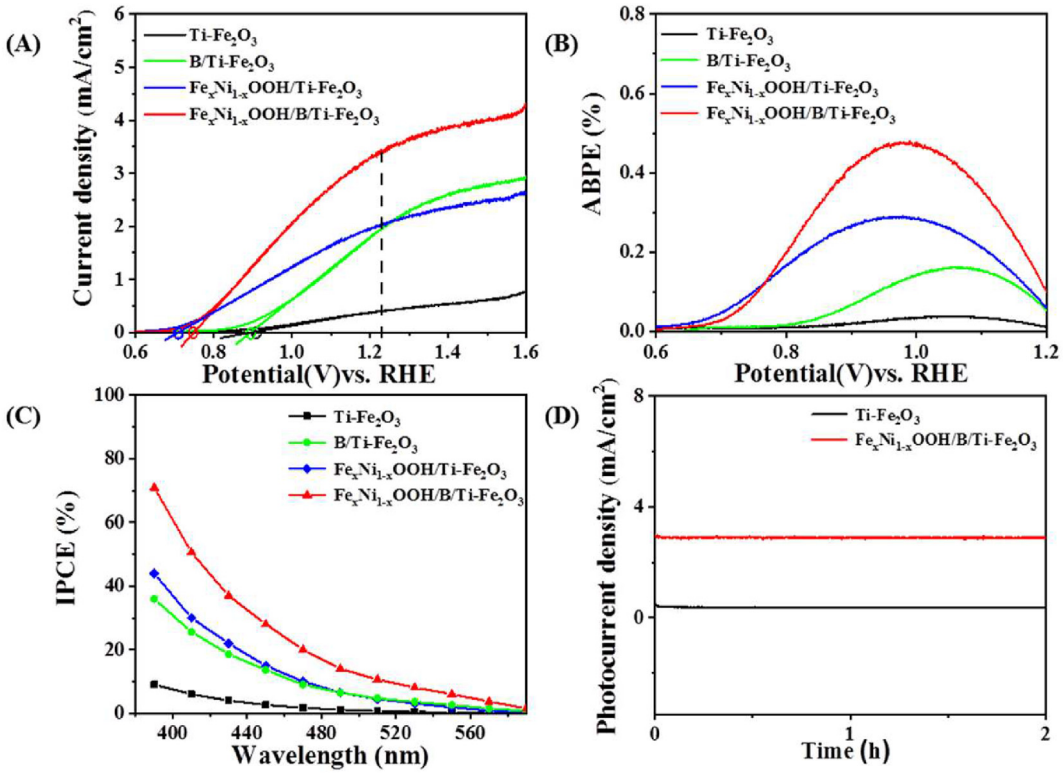

Fig. 3 – (A) LSV curves in 1 M KOH under AM 1.5 G illumination, (B) Applied bias photon-to-current efficiencies (ABPE), (C) Incident photon-current efficiency (IPCE) at 1.23 V vs. RHE of four photoanodes. (D) Photostability measurement of $Fe_xNi_{1-x}OOH/B/Ti–Fe_2O_3$ photoanode at 1.23 V vs. RHE for 2 h.

$Fe2p_{1/2}$ of Fe^{3+} [26]. In Fig. 2C, hydroxide (OH^-) and lattice oxygen (O^{2-}) correspond to two peaks at 529.7 eV and 531.1 eV, respectively [27]. It is worth noting that the peak intensity of OH^- increased significantly after borate treatment, which could be attributed to absorption of $[B(OH)_4]^-$ or OH^-. Fig. 2D shows the XPS spectrum of Ti $2p_{3/2}$ and Ti $2p_{1/2}$ of Ti^{4+}. The peaks at around 855.8 and 873.7 eV in Fig. S2A are marked as the characteristic positions of Ni $2p_{3/2}$ and Ni $2p_{1/2}$ of Ni^{2+}, respectively, while the broad peaks at 861.7 and 880.1 eV serve as their satellite peaks. In the borate-surface-treated sample(Fig. S2B), the weak B 1s XPS signal at 192.4 eV indicates that boron is a light element that cannot be easily detected [28].

PEC properties for water splitting

The PEC performance of $Ti–Fe_2O_3$, $B/Ti–Fe_2O_3$, $Fe_xNi_{1-x}OOH/Ti–Fe_2O_3$ and $Fe_xNi_{1-x}OOH/B/Ti–Fe_2O_3$ are tested with AM 1.5 G solar illumination. The photocurrent density of $B/Ti–Fe_2O_3$ (2.0 mA/cm^2) in Fig. 3A is much higher than that of $Ti–Fe_2O_3$ (0.4 mA/cm^2) at 1.23 V vs. RHE. And the optimized $B/Ti–Fe_2O_3$ is treated with 1 M borate solution for 1 h (Figs. S3A–C). The effects of other salt ion treatments such as NaOAc, phosphate buffered saline or sodium hydroxide were also compared in Fig. S3D. It's not hard to find $[B(OH)_4]^-$ has a more significant effect on the PEC performance of $Ti–Fe_2O_3$ [29]. In the precursor solution of $Fe_xNi_{1-x}OOH$, the optimal used ratio of Fe:Ni is 0.625:0.375 (Fig. S9), and a higher photocurrent density (3.39 mA/cm^2 at 1.23 V vs. RHE) was obtained by $Fe_xNi_{1-x}OOH/B/Ti–Fe_2O_3$ photoanode, much higher than most Fe_2O_3-based photoanodes (Table S1). The onset potential of $Fe_xNi_{1-x}OOH/B/Ti–Fe_2O_3$ cathodically shifted to 0.85 from 0.95 V vs. RHE ($Ti–Fe_2O_3$) in 1 M KOH electrolyte (Fig. S4). From parallel experiments, the cooperation between borate treatment and FexNi1-xOOH further improves the PEC performance.

Moreover, applying the bias photon-current efficiency (ABPE) in Fig. 3B, calculated from the J-V curves, showed that $Fe_xNi_{1-x}OOH/B/Ti–Fe_2O_3$ achieved the highest ABPE value of 0.48%, which is 1.7 times that of $Fe_xNi_{1-x}OOH/Ti–Fe_2O_3$ and 3 times that of $B/Ti–Fe_2O_3$, respectively. Then, the incident photon-current efficiency (IPCE) was obtained by the relationship between the photoelectrochemical performance and the incident light wavelength. $Fe_xNi_{1-x}OOH/B/Ti–Fe_2O_3$ achieved the highest IPCE value of 71% over the entire region in Fig. 3C. Compared with $Ti–Fe_2O_3$, $Fe_xNi_{1-x}OOH/B/Ti–Fe_2O_3$ can maintain approximately 93% of the initial photocurrent density after 2 h photostability measurement in Fig. 3D, indicating its stability during the reaction.

SEM images (Fig. S1) and XRD patterns (Fig. 2A) of $B/Ti–Fe_2O_3$ were not significantly different from that of $Ti–Fe_2O_3$. All photoanodes in Fig. 4 also exhibited similar absorption edges at 600 nm through UV/Vis absorption spectra, indicating that light absorption is not the dominant factor. The above results suggest that borate species may change the surface state of $Ti–Fe_2O_3$, inhibit surface charge recombination, while $Fe_xNi_{1-x}OOH$ thin layer with more active sites may extract holes from $B/Ti–Fe_2O_3$ to accelerate the water oxidation reaction.

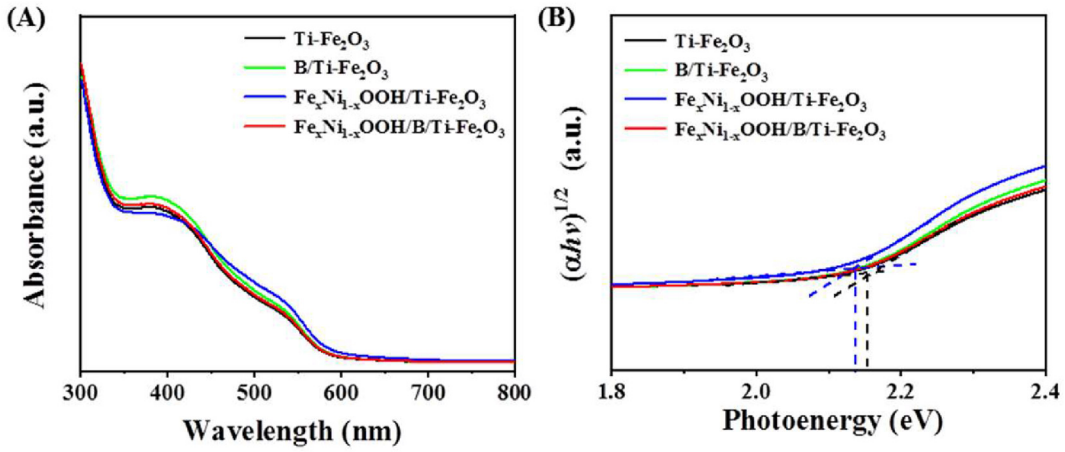

Fig. 4 – UV/Vis absorption spectra (A) and the Tauc's plots (B) of Ti–Fe_2O_3, B/Ti–Fe_2O_3, $Fe_xNi_{1-x}OOH$/Ti–Fe_2O_3 and $Fe_xNi_{1-x}OOH$/B/Ti–Fe_2O_3 photoanodes.

Enhancement of charge separation after borate treatment

To explore the change of surface state on Ti–Fe_2O_3 after borate treatment and the role of $[B(OH)_4]^-$, transient surface photovoltage spectroscopy (TPV) were conducted (Fig. 5). It is generally believed that a positive TPV response indicates the migration of photogenerated holes to the surface, while a negative response signal indicates the accumulation of photogenerated electrons on the surface [27,30]. The Ti–Fe_2O_3 photoanode obtains two TPV response signal peaks under 532 nm (~2.3 eV) pulsed laser irradiation, indicating that two distinct photogenerated charge transfer processes occur sequentially.

Firstly, the TPV response reached one negative maximum value (2.3×10^{-7} s) for Ti–Fe_2O_3 photoanode, which means the photogenerated electrons are preferentially captured by the acceptor surface states. Then, more photogenerated holes migrate to the surface under the space charge region, which the negative photovoltage response is converted into the positive photovoltage response [31]. In contrast, the negative transient photovoltage response of B/Ti–Fe_2O_3 obviously disappears, indicating that the adsorbed Lewis base $[B(OH)_4]^-$ could act as passivator to greatly reduce the acceptor surface states and inhibit charges recombination [32]. The above result confirms the type of surface state on the Ti–Fe_2O_3 surface, as reported by Lan [23] and Wu [31] et al., and it is beyond doubt that it can act as a Lewis acid site. Meanwhile, the degree of photogenerated charge separation can also be seen according to the TPV response intensity. It is evident from Fig. 5 the recombination time is prolonged from 3.7×10^{-4} s to 2×10^{-3} s after the surface passivation, which indicates that selectively passivating the acceptor surface states can significantly suppress the charge recombination centers, thus promoting charge separation more than $Fe_xNi_{1-x}OOH$ cocatalyst.

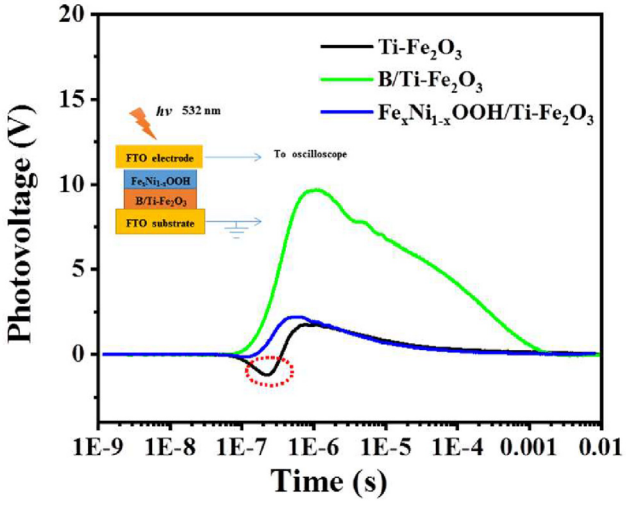

Fig. 5 – Transient surface photovoltage spectroscopy under 100 μJ laser (Laser wavelength: 532 nm, the inset is a diagram of the setup) of the Ti–Fe_2O_3, B/Ti–Fe_2O_3, $Fe_xNi_{1-x}OOH$/Ti–Fe_2O_3 photoanodes.

To further investigate the separation degree of charges after co-modification, we performed surface photovoltage spectrum (SPV), the open circuit photovoltage and photoluminescence spectrum of the obtained photoanodes. In Fig. 6A, the SPV positive response of B/Ti–Fe_2O_3 is the strongest, indicating that charge separation is easier after acceptor surface state passivation [33]. Interestingly, the SPV value of $Fe_xNi_{1-x}OOH$/B/Ti–Fe_2O_3 is poorer than that of B/Ti–Fe_2O_3 due to the introduction of interfacial resistance. On the other hand, we measured the open-circuit photovoltage (OPV) in 1 M KOH electrolyte [34,35]. The OPV values in Fig. 6B increase in order of $Fe_xNi_{1-x}OOH$/Ti–Fe_2O_3 (0.11 V) < Ti–Fe_2O_3 (0.13 V) < B/Ti–Fe_2O_3 (0.15 V) < $Fe_xNi_{1-x}OOH$/B/Ti–Fe_2O_3 (0.19 V), proving that after borate treatment, a stronger interfacial electric field is formed between the solid and liquid, and the cocatalyst further promotes charge separation. Photoluminescence (PL) also revealed the separation of photogenerated charges before and after borate treatment. In Fig. S5, the intensity of B/Ti–Fe_2O_3 was much poorer than that of Ti–Fe_2O_3, which means the charge recombination is effectively suppressed [36].

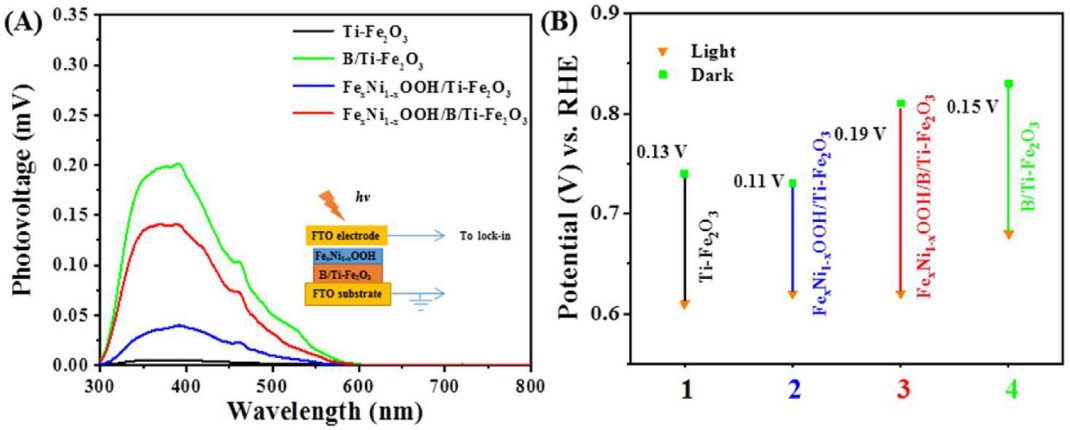

Fig. 6 – (A) Surface photovoltage spectra (the inset is a diagram of the setup), (B) Open-circuit potentials (V_{OC}) of Ti–Fe_2O_3, B/Ti–Fe_2O_3, $Fe_xNi_{1-x}OOH$/Ti–Fe_2O_3 and $Fe_xNi_{1-x}OOH$/B/Ti–Fe_2O_3 photoanodes.

Accelerated water oxidation kinetics and charge transfer after co-modification

To further analyze the congestion of holes on the surface, we measured the transient photoresponse of four photoanodes (Fig. 7A). Due to the poor water oxidation rate of Ti–Fe_2O_3, the photogenerated holes reaching the surface cannot oxidize water in time and accumulate when the light is turned on, and the photocurrent reaches instantaneous spike [37]. After the co-modification of borate treatment and $Fe_xNi_{1-x}OOH$ thin layer, the anodic spike of $Fe_xNi_{1-x}OOH$/B/Ti–Fe_2O_3 almost completely disappeared, indicating that it facilitated more holes transport from the photoanode to the electrolyte in Fig. 7B and Fig. S6.

Furthermore, the different photoanode/electrolyte interfaces resistance (R_{ct}) was obtained by electrochemical impedance spectroscopy (EIS). Generally speaking, the smaller the arc radius of the Nyquist point in the low frequency region, the smaller the charge transfer resistance between the solid-liquid interface. In Fig. 7C, the Ti–Fe_2O_3 photoanode exhibits a larger semicircle, indicating a higher interfacial transfer barrier, while the R_{ct} of $Fe_xNi_{1-x}OOH$/B/Ti–Fe_2O_3 is

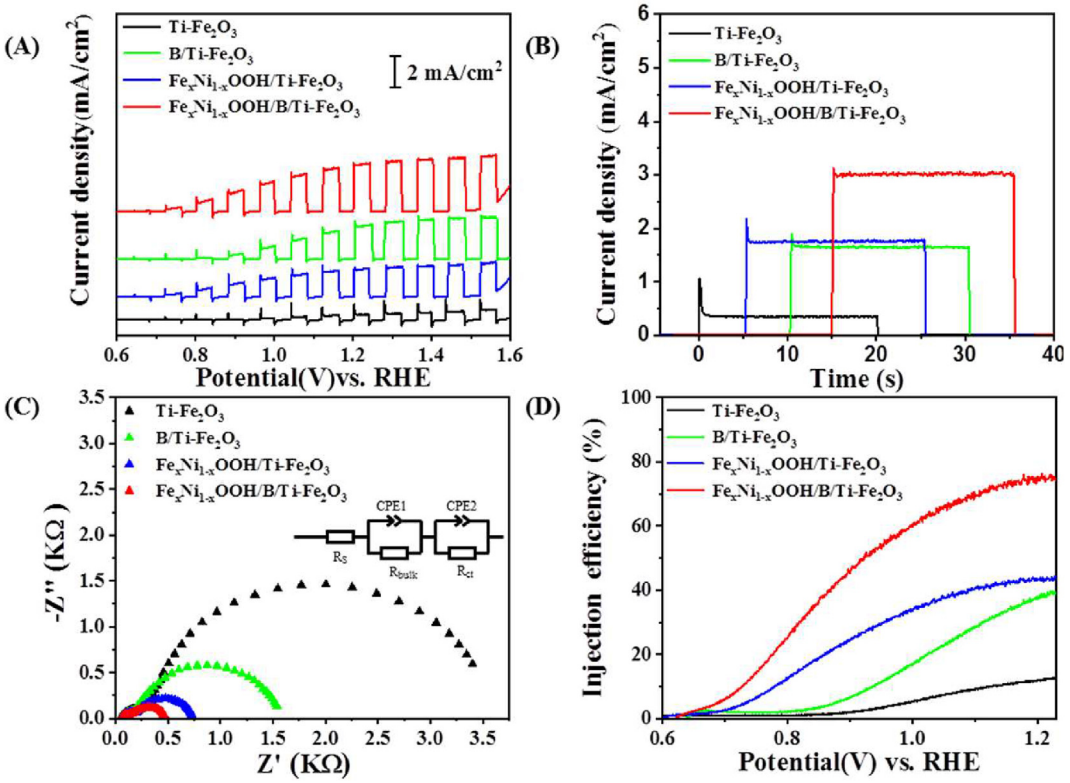

Fig. 7 – (A) J-Vcurves under chopped light illumination, (B) J-t curves at 1.23 V vs. RHE, (C) Nyquist plots at 1.0 V vs. RHE under AM 1.5G illumination (CPE, R_{ct}, and R_{bulk} represent capacitive elements, solid-liquid interface resistance and bulk resistance, respectively) and (D) η_{inj} of four photoanodes.

Table 1 – EIS fitting results of Ti–Fe_2O_3, B/Ti–Fe_2O_3, $Fe_xNi_{1-x}OOH$/Ti–Fe_2O_3 and $Fe_xNi_{1-x}OOH$/B/Ti–Fe_2O_3 photoanodes.

Photoanode	Rs(Ω)	Rbulk (Ω)	CPE1(F.cm^{-2})	R_{ct} (Ω)	CPE2(F.cm^{-2})
Ti–Fe_2O_3	60.25	236	2.167×10^{-5}	3362	1.795×10^{-4}
B/Ti–Fe2O3	42.94	145.7	5.347×10^{-5}	1383	2.077×10^{-4}
$Fe_xNi_{1-x}OOH$/Ti–Fe2O3	49.79	148.5	2.988×10^{-5}	539.8	3.392×10^{-4}
$Fe_xNi_{1-x}OOH$/B/Ti–Fe_2O_3	53.11	82.75	5.761×10^{-5}	348.9	6.852×10^{-4}

significantly smaller. Compared with $Fe_xNi_{1-x}OOH$/Ti–Fe_2O_3, the radius of $Fe_xNi_{1-x}OOH$/B/Ti–Fe_2O_3 in high frequency region is obviously smaller in Fig. S7, indicating that the passivation of the acceptor surface states reduces the transfer resistance of holes from Ti–Fe_2O_3 to the surface of $Fe_xNi_{1-x}OOH$. Moreover, the fitted values obtained from the equivalent circuit model are shown in Table 1. The fitted R_{ct} (384.9 Ω) of the $Fe_xNi_{1-x}OOH$/B/Ti–Fe_2O_3 photoanode is significantly smaller than that of the B/Ti–Fe_2O_3 photoanode (1383 Ω), indicating that the photogenerated holes on the surface of $Fe_xNi_{1-x}OOH$/B/Ti–Fe_2O_3 are transported more smoothly at the solid-liquid interface, which can be quickly injected into the electrolyte for water oxidation reaction [38].

In view of the above results, the hole injection efficiencies (η_{inj}) of the four photoanodes in Fig. 7D, were further calculated from the photocurrent measurements with H_2O_2 [39]. $Fe_xNi_{1-x}OOH$/B/Ti–Fe_2O_3 photoanode manifested the highest value of 74% at 1.23 V vs. RHE, much higher than that of B/Ti–Fe_2O_3 (39%) and Ti–Fe_2O_3 (12%). The excellent injection efficiency of $Fe_xNi_{1-x}OOH$/B/Ti–Fe_2O_3 means that more holes are involved in the reaction of oxidizing water, which can be attributed to the passivation of acceptor surface states inhibiting charge recombination, and the cocatalyst $Fe_xNi_{1-x}OOH$ with more active sites can rapidly extract holes from B/Ti–Fe_2O_3 to electrolyte [40]. The same results were also observed in the EIS spectrum and LSV test.

To further unveil the reason of excellent photoelectrochemical performance of $Fe_xNi_{1-x}OOH$/B/Ti–Fe_2O_3, we have approximately evaluated its electrochemical active surface area (ECSA) according to the electrochemical double-layer capacitance (C_{dl}) [41,42]. It should be noted that C_{dl} should be calculated by monitoring the current density in the non redox peak area at different scanning rates (Figs. S10A–C). Obviously, the C_{dl} of $Fe_xNi_{1-x}OOH$/B/Ti–Fe_2O_3 (37 m F cm^{-2}) is much higher than that of B/Ti–Fe_2O_3 (21 m F cm^{-2}) and Ti–Fe_2O_3 (12 m F cm^{-2}) in Fig. S10D, which shows that $Fe_xNi_{1-x}OOH$/B/Ti–Fe_2O_3 exposes the highest active sites due to the passivation of surface state and the presence of $Fe_xNi_{1-x}OOH$. This results further indicate that the synergetic integration of acceptor surface states passivation and $Fe_xNi_{1-x}OOH$ cocatalyst provides a new strategy for improving the photoelectrochemical properties of Fe_2O_3 for water oxidation.

Analysis of the charge migration mechanism in the reaction

The reaction mechanism in the process, therefore, is proposed in Scheme 2. For the Ti–Fe_2O_3, photogenerated electrons from the conduction band are preferentially captured by acceptor surface states, and then they recombine with holes from the valence band, severely limiting the water oxidation reaction (Scheme 2A). After Lewis base $[B(OH)_4]^-$ gradually interacts with the acceptor surface state on the Ti–Fe_2O_3 surface, the

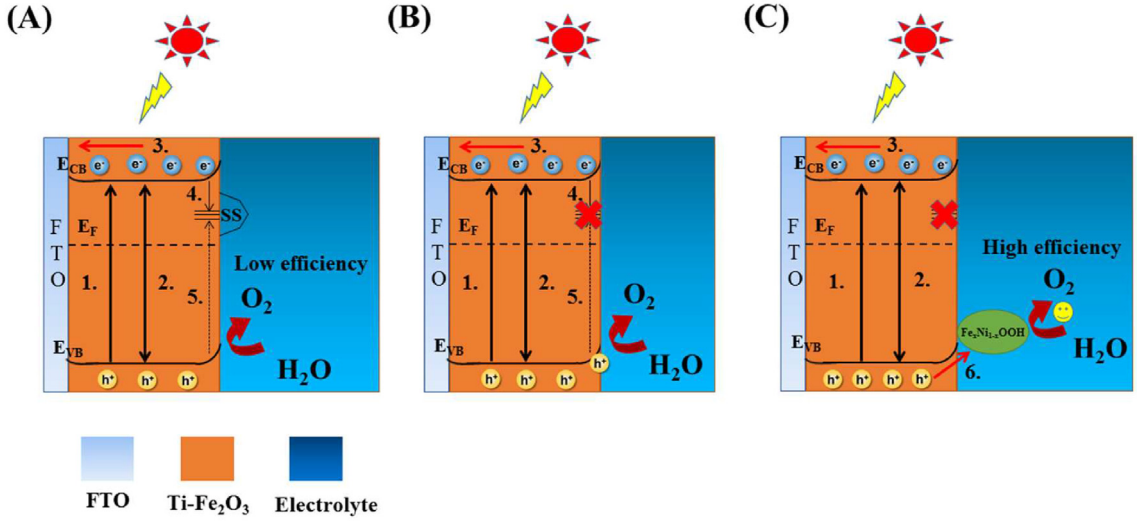

Scheme 2 – The illustration of reaction mechanism of (A) Ti–Fe_2O_3, (B) B/Ti–Fe_2O_3 photoanodes and (C) $Fe_xNi_{1-x}OOH$/B/Ti–Fe_2O_3. Each process represents: 1. Formation of photogenerated charges, 2. Nonradiative recombination of photogenerated electron-hole pairs, 3. Electrons transfer to conductive substrates, 4. Electrons captured by the acceptor surface states, 5. Acceptor surface states as recombination centers, 6. Hole-transport to the $Fe_xNi_{1-x}OOH$ cocatalyst overlayer.

recombination center is inhibited, thereby promoting more electron-hole pairs separation (Scheme 2B). Finally, when the surface of B/Ti–Fe_2O_3 is decorated with $Fe_xNi_{1-x}OOH$ thin layer possessing more active sites, holes can be rapidly participated to the water oxidation reaction, thus accelerating the OER reaction kinetics (Scheme 2C).

Conclusions

In summary, $Fe_xNi_{1-x}OOH$/B/Ti–Fe_2O_3 greatly improved the performance of Ti–Fe_2O_3 photoanode. Firstly, borate treatment can efficiently suppress charges recombination through the selective passivation of the acceptor surface states, and secondly, the modification of $Fe_xNi_{1-x}OOH$ can further improve the efficiency of photogenerated holes injection into the electrolyte, accelerating the water oxidation kinetics of Ti–Fe_2O_3. The photocurrent density of $Fe_xNi_{1-x}OOH$/B/Ti–Fe_2O_3 photoanode (3.39 mA/cm^2 at 1.23 V vs. RHE) shows a 8.5-fold increasement when compared with that of Ti–Fe_2O_3 photoanode (0.4 mA/cm^2 at 1.23 V vs. RHE). The synergetic integration of acceptor surface states passivation and $Fe_xNi_{1-x}OOH$ cocatalyst provides a new strategy for the construction of efficient PEC photoanodes by surface engineering.

Declaration of competing interest

The authors declare that they have no known competing financial interests or personal relationships that could have appeared to influence the work reported in this paper.

Acknowledgements

This work was financially supported by the National Natural Science Foundation of China (Grant Nos. 22172057, 21773086, 21872063).

Appendix A. Supplementary data

Supplementary data to this article can be found online at https://doi.org/10.1016/j.ijhydene.2022.10.277.

REFERENCES

[1] Yu X, Liu J, Yin W, Wang T, Quan L, Ran Y, Cui J, Wang L, Zhang Y. Appl Surf Sci 2019;492:264–71.
[2] Wu J, Qi M, Wang G, Yu B, Liu C, Hou W, Liu W. ACS Sustainable Chem Eng 2020;8:5200–8.
[3] Fujishima A, Honda K. Nature 1972;238:37–8.
[4] Bu Q, Li S, Wu Q, Lin Y, Wang D, Zou X, Xie T. Catal Sci Technol 2019;9:5812–8.
[5] Xing X, Bao M, Wang P, Wang X, Wang Y, Du J. Appl Surf Sci 2022;572:151472.
[6] Li J, Wan W, Triana C, Chen H, Zhao Y, Mavrokefalos C, Patzke G. Nat Commun 2021;12:255.
[7] Tang P, Arbiol J. Nanoscale Horiz 2019;4:1256–76.
[8] Zhang X, Wang X, Yi X, Ye J, Wang D. ACS Sustainable Chem Eng 2019;7:5420–9.
[9] Kubendhiran S, Chung R, Yougbar S, Lin L. Int J Hydrogen Energy 2022;47:27012–22.
[10] Ji H, Shao S, Yuan G, Lu C, Feng K, Xia Y, Lv X, Zhong J, Xu H, Deng J. J Energy Chem 2021;52:147–54.
[11] Li H, Wang Z, Jing H, Yi S, Zhang S, Yue X, Zhang Z, Lu H, Chen D. Appl Catal B Environ 2021;284:119760.
[12] McDonald K, Choi K. Chem Mater 2011;23:4863–9.
[13] Ji H, Shao S, Yuan G, Lu C, Feng K, Xia Y, Lv X, Zhong J, Xu H, Deng J. J Energy Chem 2021;52:147–54.
[14] Lamers M, Fiechter S, Friedrich D, Abdi FF, van de Krol R. J Mater Chem 2018;6:18694–700.
[15] Zhang B, Huang X, Zhang Y, Lu G, Chou L, Bi Y. Angew Chem Int Ed 2020;59:18990–5.
[16] Huang J, Luo W, Ma W, Yuan X. Int J Hydrogen Energy 2022;47:17600–10.
[17] Deng J, Zhang Q, Feng K, Lan H, Zhong J, Chaker M, Ma D. ChemSusChem 2018;11:3783–9.
[18] Liardet L, Katz J, Luo J, Atzel M, Hu X. J Mater Chem 2019;7:6012–20.
[19] Wu D, Zhang Z. Electrochim Acta 2018;282:48–55.
[20] Fu Z, Jiang T, Zhang L, Liu B, Wang D, Wang L, Xie T. J Mater Chem 2014;2:13705–12.
[21] Hisatomi T, Formal F, Cornuz M, Brillet J, Tétreault N, Sivula K, Grätzel M. Energy Environ Sci 2011;4:2512–5.
[22] Anushkkaran P, Dhandole L, Chae W, Lee H, Choi S, Ryu J, Jang J. Int J Hydrogen Energy 2022;47:32015–30.
[23] Lan H, Wei A, Zheng H, Sun X, Zhong J. Nanoscale 2018;10:7033.
[24] Bu Q, Li S, Zhang K, Lin Y, Wang D, Zou X, Xie T. ACS Sustainable Chem Eng 2019;7:10971–8.
[25] Reddy D, Reddy K, Gopannagari M, Kim Y, Kumar D, Kim T. Appl Surf Sci 2021;570:151134.
[26] Xi L, Bassi P, Chiam S, Mak W, Tran P, Barber J, Loo J, Wong L. Nanoscale 2012;4:4430–3.
[27] Li Y, Zhang R, Li C, Li H, Fang Q, Xie T. J Colloid Interface Sci 2022;608:1449–56.
[28] Zhang J, Huang Y, Lu X, Yang J, Tong Y. ACS Sustainable Chem Eng 2021;9:8306–14.
[29] Meng Q, Zhang B, Fan L, Liu H, Valvo M, Edstrçm K, Cuartero M, Marco R, Crespo G, Sun L. Angew Chem Int Ed 2019;58:19027–33.
[30] Takashima T, Ishikawa K, Irie H. J Phys Chem C 2016;120:24827–34.
[31] Wu Q, Meng D, Zhang Y, Zhao Q, Bu Q, Wang D, Zou X, Lin Y, Li S, Xie T. J Alloys Compd 2019;782:943–51.
[32] Bu Q, Li S, Wu Q, Bi L, Lin Y, Wang D, Zou X, Xie T. ChemSusChem 2018;11:3486–94.
[33] Zhang R, Wang H, Li Y, Wang D, Lin Y, Li Z, Xie T. ACS Sustainable Chem Eng 2021;9:7286–97.
[34] Li Y, Chen Y, Wu Q, Zhang R, Li M, Lin Y, Wang D, Xie T. Catal Sci Technol 2022;12:250.
[35] Liua C, Xua Y, Luo H, Wang W, Liang Q, Chen Z. Chem Eng J 2019;363:23–32.
[36] Li M, Zhang G, Feng C, Wu H, Mei H. Sensor Actuator B Chem 2020;305:127449.
[37] Fan Z, Xu Z, Yan S, Zou Z. J Mater Chem 2017;5:8402–7.
[38] Chen D, Liu Z. ChemSusChem 2018;11:3438–48.
[39] Yuan Y, Gu J, Ye K, Chai Z, Yu X, Chen X, Zhao C, Zhang Y, Mai W. ACS Appl Mater Interfaces 2016;8:16071–7.
[40] Lin Y, Fang W, Xv R, Fu L. Int J Hydrogen Energy 2022;47:33361–73.
[41] Zhang R, Li L, Li Y, Wang D, Lin Y, Xie T. Sol. RRL 2022:2200536.
[42] Ruan X, Cui X, Cui Y, Fan X, Li Z, Xie T, Ba K, Jia G, Zhang H, Zhang L, Zhang W, Zhao X, Leng J, Jin S, Singh D, Zheng W. Adv Energy Mater 2022;12:2200298.